Predictive Control Strategy for an Induction Machine fed by a 3L-NPC Converter with Fixed Switching Frequency and Improved Tracking Error

Andrés Mora*, Felipe Donoso*, Matías Urrutia*, Alejandro Angulo* and Roberto Cárdenas†
*Departamento de Ingeniería Eléctrica, Universidad Técnica Federico Santa María, Chile
† Departamento Ingeniería Eléctrica, Universidad de Chile, Chile
Email: a.mora@ieee.org

***Abstract*—In this paper, a model predictive control (MPC) strategy to drive an induction machine (IM) using a three-level neutral point-clamped (3L-NPC) converter is investigated. The proposed strategy is a space vector modulation based MPC which controls the torque and flux of the IM by using a cost function focusing on the average tracking error of the stator flux linkage vector. Simulation results show an improved steady-state performance maintaining the fast dynamic response of the standard finite control set MPC. The control strategy works appropriately with a relatively low sampling frequency of 1 kHz, and it exhibits zero average tracking error in the controlled variables.**

***Index Terms*—model predictive control, space vector modulation, multilevel converter.**

I. Introduction

Control schemes for power converters and drives have been constantly evolving according with the development of new semiconductor devices and the introduction of new control platforms. Nowadays, with the development of more powerful microprocessors, new control schemes have been proposed for power converters and drives. Among these new controllers, predictive control seems to be an useful alternative due to its ability to include non linearities, its fast transient response, and ease inclusion of constraints [1].

In the context of power electronics, one of the most attractive predictive control strategies is the so-called finite control set MPC (FCS-MPC) [2]. This control strategy uses the discrete nature of power converters to define a finite set of switching actions. To obtain the optimal one, the variables to be controlled are predicted and a cost function is evaluated for every feasible converter switching state. The optimal switching action, which minimized the cost function, is applied during the whole next sampling period. Consequently, modulation stages are not required. As evidenced in the literature [2, 3], FCS-MPC has proved to be an interesting alternative for controlling power converters since it is relatively simple to include nonlinearities, constraints, and variable of different nature in the cost function. Nevertheless, FCS-MPC operates with variable switching frequency, generating a dispersed harmonic spectrum. This operating feature leads, in general, to more significant ripple than techniques that include modulation stages at similar switching frequencies [4]. Moreover, FCS-MPC controller produces, in general, a nonzero average steady-state tracking error [3, 5].

To overcome these difficulties, the Multistep FCS-MPC (or FCS-MPC with long horizons) for power electronics has been recently presented in [6, 7] for multilevel topologies. To find efficiently the optimal switching sequence, the optimization problem is reformulated in terms of the unconstrained solution to apply the sphere decoding algorithm. Under this predictive strategy, the steady-state performance has been certainly improved. However, the maximum number of nodes to be evaluated in each sampling period for this algorithm has not a deterministic upper bound that guarantees its execution during the available processing time.

On the other hand, to improve the performance of the FCS-MPC, recently, the space vector modulation (SVM) has been integrated into several predictive control algorithms [8–11]. In [9], the method is named as Modulated-MPC and, it is able to operate with fixed switching frequency without losing the advantages of standard FCS-MPC strategy. However, the duty-cycles are obtained using a heuristic procedure which, in general, may lead to an undesirable performance of the converter. A similar strategy is used in [12] to control a grid-connected 3L-NPC converter. Here, the predictive control is designed to regulate the current supplied to the grid using a single-objective cost function while the capacitor voltage balancing is achieved by utilizing the redundancy states of the converter [13]. Moreover, in [10], a control scheme is presented for a two-level converter driving permanent-magnet motors. In this strategy, the pair of active vectors are selected by performing some geometrical considerations, and their duty-cycles are computed by using a linear combination of the prediction errors produced by them and the zero vector. The resulting voltage vector is restricted to the linear range of the modulator; and hence, the control technique may lead to suboptimal solutions, especially in the transient operation.

This paper proposes a generic strategy for calculating the duty-cycles when a SVM strategy is added into the FCS-MPC algorithm. The controller is applied to a medium-voltage high-power induction machine (IM), and it is focused on minimizing the average stator flux tracking error when the 3L-NPC converter applies a seven-segment switching sequence. The controller computes a locally optimal solution for all

978-1-5386-3705-0/18/$31.00 ©2018 IEEE

sections in which the control region is divided and the optimal section with its corresponding duty-cycles are obtained by using an enumeration algorithm. In addition, a saturation scheme dealing with the system constraints is also proposed. The performance of the technique is evaluated with simulation results in a high-power induction machine fed by a medium-voltage 3L-NPC converter.

II. Description of the Drive

A. Model of the Converter

The circuit diagram of a typical 3L-NPC converter is shown in Fig. 1(a). The converter is composed of four switches and two clamped diodes per leg which produce 27 three-phase switching valid states $\boldsymbol{u}_{abc}\in\{-1,0,1\}^3$. As shown in Fig. 1(b), these switching states generate 19 non-redundant and 8 redundant switching vectors in the stationary $\alpha\beta$ by using the transformation $\boldsymbol{u}_{\alpha\beta}=\boldsymbol{\mathcal{T}}\boldsymbol{u}_{abc}$, with

$$\boldsymbol{\mathcal{T}}=\frac{2}{3}\begin{bmatrix}1 & -\frac{1}{2} & -\frac{1}{2}\\ 0 & \frac{\sqrt{3}}{2} & -\frac{\sqrt{3}}{2}\end{bmatrix}. \tag{1}$$

The small vectors [red dots in Fig. 1(b)] play a significant role in balancing the capacitor voltages since, for each of them, its single-redundancy produces the same line-to-line voltage with a NP-current of the same amplitude but opposite direction. This principle allows balancing the capacitor voltages without sacrificing the quality of the output currents by redistributing the dwell times of the small switching vectors [12, 13].

To satisfy the minimum switching transition principle, direct switching between the states +1 and -1 in each leg is prohibited [13]. Thereby, as shown Fig. 1(b), the whole control region in the stationary $\alpha\beta$ frame is typically divided into six sectors, each of which is subdivided into four regions, forming 24 convex sets named as $\mathcal{R}\in\mathbb{S}\triangleq\{\mathcal{R}_1,\ldots,\mathcal{R}_{24}\}$. These convex sets are defined by any convex combination of the three nearest switching vectors accomplishing the minimum switching principle. The order in which the converter applies these vectors within a sampling cycle is known as switching sequence (SSq).

Taking into account the influence of small vectors in the capacitor voltages balancing problem, it is desirable to begin the switching sub-cycle period with a small vector, $\boldsymbol{u}_s$, and to end it with its single-redundancy $\boldsymbol{u}'_s$ [13]. The seven-segment SSq can be defined accordingly for all regions $\mathcal{R}\in\mathbb{S}$ as:

$$\begin{aligned}\boldsymbol{S}:=\Big\{&\boldsymbol{u}_s[d_1],\boldsymbol{u}_2[d_2],\boldsymbol{u}_3[d_3],\boldsymbol{u}'_s[d_4],\cdots\\ &\boldsymbol{u}'_s[d_4],\boldsymbol{u}_3[d_3],\boldsymbol{u}_2[d_2],\boldsymbol{u}_s[d_1]\Big\}\end{aligned} \tag{2}$$

with d_j the normalized dwell-time in which the jth switching vector is applied by the converter. In consequence, the aim of the proposed controller is to define both the optimal switching sequence and its corresponding duty-cycles.

B. Model Predictive Stator-Flux Control (MP-SFC)

The stator flux linkage vector $\boldsymbol{\psi}_s$ is adopted in this work to accomplish torque and flux control of an IM. The electromagnetic torque is given by [14]

$$T_e=k_{\mathrm{T}}\|\boldsymbol{\psi}_s\|\|\boldsymbol{\psi}_r\|\sin(\theta_s-\theta_r), \tag{3}$$

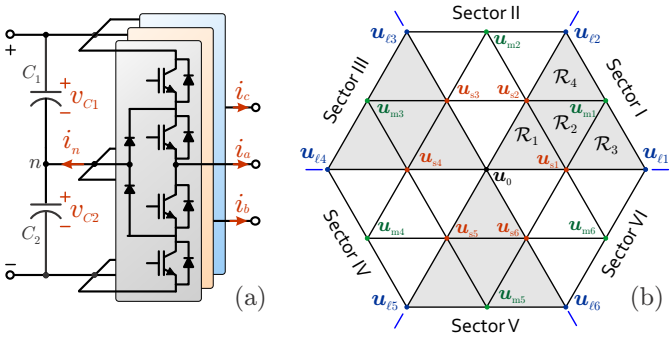

Fig. 1. 3L-NPC converter: (a) topology; (b) space of vectors.

with $k_{\mathrm{T}}=\frac{3}{2}p\frac{L_m}{\sigma L_s L_r}$, and $\theta_{s(r)}$ the stator(rotor) flux angle measured from a common reference frame. A fast torque control can be achieved by manipulating θ_s while the magnitudes of the stator and rotor flux vectors are kept constant. Notice that thanks to the large rotor time constant, both the magnitude and the angular position of the rotor flux vector can be considered constant during the transient process in which the torque expression is evaluated. Thus, by assuming that the magnitude of the stator flux $\Psi_s=\|\boldsymbol{\psi}_s\|$ is controlled around its nominal value Ψ_s^*, for a given torque reference T_e^*, the desired angular position of the stator flux can be determined as:

$$\theta_s^*=\theta_r+\arcsin\left(\frac{T_e^*}{k_{\mathrm{T}}\Psi_s^*\|\boldsymbol{\psi}_r\|}\right) \tag{4}$$

Therefore, the control target is accomplished if the stator flux vector is manipulated according to

$$\boldsymbol{\psi}_s^*=\Psi_s^*\begin{bmatrix}\cos\theta_s^*\\ \sin\theta_s^*\end{bmatrix} \tag{5}$$

The overall control scheme is depicted in Fig. 2. Here, the torque reference T_e^* is provided by the speed controller and the rotor flux $\boldsymbol{\psi}_r$ is estimated from the dynamic model of the IM by using both the stator current vector and speed measurement ω. Using $\boldsymbol{\psi}_r$, T_e^* and Ψ_s^*, the reference generator block computes the desired stator flux vector by evaluating (4) and (5). Then, the reference and the predictions of the stator flux are somehow compared by using a proper cost function from which the optimal SSq with its corresponding duty-cycle is obtained. The proposed control strategy is further discussed in the following section.

III. Switching-Sequence Set MPC

Typically in FCS-MPC strategies, the optimal control action is derived from the minimization of a cost function that compares the reference and the prediction of the variables to be controlled at the end of the sampling period. In a different manner, this paper proposes using the prediction of the average stator flux trajectory over the next switching cycle when the converter applies a SSq as (2) to the IM.

For this purpose, let us consider the stator winding dynamic equation in stationary coordinates,

$$\frac{\mathrm{d}\boldsymbol{\psi}_s}{\mathrm{d}t}=\boldsymbol{v}_s-R_s\boldsymbol{i}_s, \tag{6}$$

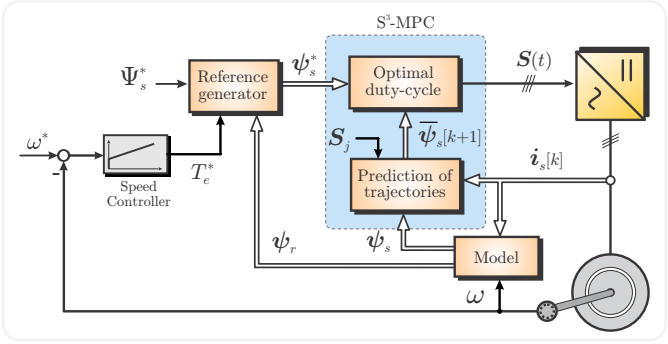

Fig. 2. Predictive stator flux controller to drive an IM.

where $\boldsymbol{v}_s{=}[v_{s\alpha}\ v_{s\beta}]^\intercal$ and $\boldsymbol{i}_s{=}[i_{s\alpha}\ i_{s\beta}]^\intercal$ are the stator voltage and current vectors, respectively. For high-power IMs, the stator resistance, R_s, can be neglected in (6); and consequently, the evolution of the stator flux during a switching period can be expressed as a piecewise linear function of the time, as illustrated in Fig. 3 for a seven-segment SSq (2). In this regard, and considering the symmetrical nature of the seven-segment SSq, it can be proved that the average trajectory over the whole switching cycle corresponds to the instantaneous value of the stator flux at the end of the sub-cycle, i.e., $\overline{\boldsymbol{\psi}}_s[k{+}1]{=}\boldsymbol{\psi}_{s4}$ as depicted in Fig. 3. Thereby, when the converter applies a seven-segment SSq to the IM, the average stator flux over the next switching cycle can be predicted as

$$\overline{\boldsymbol{\psi}}_s[k{+}1]{=}\boldsymbol{\psi}_s[k]{+}\Delta\boldsymbol{\psi}_{s1}d_1{+}\Delta\boldsymbol{\psi}_{s2}d_2{+}\Delta\boldsymbol{\psi}_{s3}d_3{+}\Delta\boldsymbol{\psi}_{s4}d_4 \tag{7}$$

being $\Delta\boldsymbol{\psi}_{sj}{=}T_0\boldsymbol{v}_j$, the incremental trajectory of the stator flux when the converter applies the jth voltage vector during the whole sub-cycle interval $T_0 = T_s/2$.

Assuming the capacitor voltages are balanced, the effect of each small vector and its redundancy over the stator flux is the same, i.e., $\Delta\psi_{s1} = \Delta\psi_{s4}$, leading to

$$\overline{\boldsymbol{\psi}}_s[k{+}1] = \boldsymbol{\psi}_s[k] + \frac{V_{dc}}{2}T_0\boldsymbol{U}[k]\,\boldsymbol{d}[k] \tag{8}$$

with $\boldsymbol{d}{=}\big[d_0\ d_2\ d_3\big]^\intercal{\in}[0,1]^3$, the system input to be computed by the controller, where $d_0{=}d_1{+}d_4$, and $\boldsymbol{U}{=}\big[\boldsymbol{u}_s\ \boldsymbol{u}_2\ \boldsymbol{u}_3\big]{\in}\mathbb{R}^{2\times3}$, a matrix composed by the switching vectors that define each convex set of the control region [see Fig. 1(b)].

To obtain the optimal duty-cycle, the following quadratic cost function is introduced

$$J(\boldsymbol{d}[k]) = \big\|\overline{\boldsymbol{\psi}}_s[k{+}1]{-}\boldsymbol{\psi}^*_s[k{+}1]\big\|_2^2 + \lambda_u\big\|\boldsymbol{u}[k]{-}\boldsymbol{u}[k{-}1]\big\|_2^2 \tag{9}$$

which is a suitable choice to trade stator flux tracking error versus control input effort, where

$$\boldsymbol{u}[k] = \boldsymbol{U}[k]\boldsymbol{d}[k] \tag{10}$$

is the average switching vector for a given switching cycle. In consequence, the scalar parameter $\lambda_u \geq 0$ is used to provide more robustness to the system by penalizing the size of the increments of the control input.

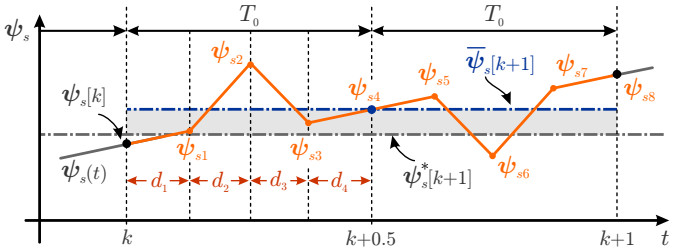

Fig. 3. Predicted stator flux trajectory for a seven-segment SSq.

Finally, for each SSq, the admissible duty-cycles are those that must be non-negative and sum one. Therefore, to obtain the optimal duty-cycle, the following simplex-constrained least-square problem (SCLS) must be solved

$$\min_{\boldsymbol{d}}\ \big\|\gamma\,\boldsymbol{U}\boldsymbol{d} - \boldsymbol{e}[k]\big\|_2^2 + \lambda_u\big\|\boldsymbol{U}\boldsymbol{d} - \boldsymbol{u}[k{-}1]\big\|_2^2 \tag{11a}$$

$$\text{s.t.}\ \ \mathbb{1}^\intercal\boldsymbol{d} = 1 \tag{11b}$$

$$d_j \geq 0 \tag{11c}$$

with $\boldsymbol{e}[k]{=}\boldsymbol{\psi}^*_s[k{+}1]{-}\boldsymbol{\psi}_s[k]$ the tracking error at the beginning of the sampling period and $\gamma = \frac{V_{dc}}{2}T_0$ a positive scalar.

A. Relaxed solution

To efficiently solve the SCLS problem (11), in this work it is proposed first to compute the solution of the relaxed problem and then, to apply a simple and suitable method to fulfil the constraint (11c). In the relaxed problem, the non-negative constraints over the duty-cycles (inequality $d_j{\geq}0$) are ignored. In consequence, the relaxed solution, denoted as $\boldsymbol{d}_\text{r}$, is the one that solves the following bi-objective constrained least-square (CLS) problem [15],

$$\min_{\boldsymbol{d}}\ \big\|\gamma\,\boldsymbol{U}\boldsymbol{d} - \boldsymbol{e}[k]\big\|_2^2 + \lambda_u\big\|\boldsymbol{U}\boldsymbol{d} - \boldsymbol{u}[k{-}1]\big\|_2^2 \tag{12}$$

$$\text{s.t.}\ \ \mathbb{1}^\intercal\boldsymbol{d} = 1,$$

Thereby, using the Lagrange method, $\boldsymbol{d}_\text{r}$ can be obtained by solving the following linear system of 4 equations:

$$\begin{bmatrix}(\gamma^2{+}\lambda_u)\boldsymbol{U}^\intercal\boldsymbol{U} & \mathbb{1}\\ \mathbb{1}^\intercal & 0\end{bmatrix}\begin{bmatrix}\boldsymbol{d}_\text{r}\\ \nu\end{bmatrix} = \begin{bmatrix}\boldsymbol{U}^\intercal(\gamma\boldsymbol{e}[k]{+}\lambda_u\boldsymbol{u}[k{-}1])\\ 1\end{bmatrix}, \tag{13}$$

whose unique solution is guaranteed since the stacked matrix $[\boldsymbol{U}^\intercal\ \mathbb{1}]^\intercal$ has linearly independent columns for all regions. Thus, the CLS is directly solved by using the inverse of the left-hand square matrix in (13). In this regard, the relaxed solution is given by:

$$\begin{bmatrix}d_{\text{r}0}\\ d_{\text{r}2}\\ d_{\text{r}3}\end{bmatrix}{=}\frac{1}{\Theta}\begin{bmatrix}b_1(u_{2\beta}{-}u_{3\beta}){+}b_2(u_{3\alpha}{-}u_{2\alpha}) + u_{2\alpha}u_{3\beta}{-}u_{2\beta}u_{3\alpha}\\ b_1(u_{3\beta}{-}u_{0\beta}){+}b_2(u_{0\alpha}{-}u_{3\alpha}) + u_{3\alpha}u_{0\beta}{-}u_{3\beta}u_{0\alpha}\\ b_1(u_{0\beta}{-}u_{2\beta}){+}b_2(u_{2\alpha}{-}u_{0\alpha}) + u_{0\alpha}u_{2\beta}{-}u_{0\beta}u_{2\alpha}\end{bmatrix} \tag{14}$$

where

$$\Theta = \boldsymbol{u}_0{\times}\boldsymbol{u}_2 + \boldsymbol{u}_3{\times}\boldsymbol{u}_0 + \boldsymbol{u}_2{\times}\boldsymbol{u}_3, \tag{15}$$

$$\begin{bmatrix}b_1\\ b_2\end{bmatrix} = \frac{1}{\gamma^2+\lambda_u}\boldsymbol{U}^\intercal\big(\gamma\boldsymbol{e}[k]{+}\lambda_u\boldsymbol{u}[k{-}1]\big) \tag{16}$$

and $\boldsymbol{u}_x{\times}\boldsymbol{u}_y = u_{x\alpha}u_{y\beta}{-}u_{x\beta}u_{y\alpha}$ denotes the cross product.

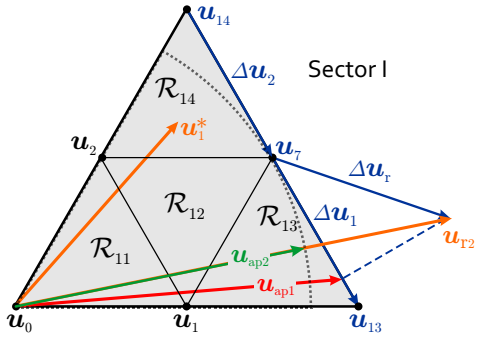

Fig. 4. Graphical representation of the two saturation schemes.

B. Handling non-negative constraints

Accordingly to the above, for each switching sequence $\boldsymbol{S}_j$, a local relaxed solution $\boldsymbol{d}_{\mathrm{r}j}$ is obtained by evaluating (14). This solution meets $\mathbb{1}^\intercal \boldsymbol{d}_r{=}1$ but all its components not necessarily are non-negative. It follows that relaxed solution can be mapped onto the $\alpha\beta$-plane wit the following affine combination

$$\boldsymbol{u}_{\mathrm{r}j} = \boldsymbol{U}_j \boldsymbol{d}_{\mathrm{r}j}, \tag{17}$$

Thereby, the global optimal solution defines a unique point in the $\alpha\beta$-plane, denoted as $\boldsymbol{u}_{\mathrm{r}}^*$.

Under the assumption that $\boldsymbol{u}_{\mathrm{r}}^*$ falls within the control region [hexagon shown in Fig. 1(b)], there exists just one region $\mathcal{R}^*$ able to generate $\boldsymbol{u}^\star$ through a convex combination of their switching vectors. This means that only one among all the local solutions has non-negative duty-cycles; and hence, it will be the global solution to the problem. As illustrated in Fig. 4(b), the only region able to produce $\boldsymbol{u}_1^*$ through a convex combination is $\mathcal{R}_{14}$. In consequence, the optimal duty-cycle $\boldsymbol{d}^*$ is directly obtained by evaluating the non-negativity condition for the three components of each relaxed solution. Under this perspective, the cost function evaluation for all regions is avoided in this work.

If conversely, $\boldsymbol{u}_{\mathrm{r}}^*$ falls out of the hexagon, there is no local solution with all its duty-cycles non-negative. To deal with this problem, two saturation schemes are introduced in this paper. In the first saturation scheme, the aim is to find a vector on the hexagon's frontier, $\boldsymbol{u}_{\mathrm{ap}}$, as close as possible to the relaxed solution. For this purpose, only the pair of switching vectors with the minimal distance to the relaxed solution $\boldsymbol{u}_{\mathrm{r}}^*$ are considered. Then, the duty-cycle associated to the small vector must be zero, i.e., $d_0{=}0$ and the duty-cycles of the large and medium vectors are respectively computed as

$$d_2 = \mathrm{mid}\left\{0, \frac{\Delta \boldsymbol{u}_{\mathrm{r}}^\intercal \Delta \boldsymbol{u}_{\mathrm{f}}}{\|\Delta \boldsymbol{u}_{\mathrm{f}}\|^2}, 1\right\} \quad ; \quad d_3{=}1{-}d_2 \tag{18}$$

with $\Delta \boldsymbol{u}_{\mathrm{r}}{=}\boldsymbol{u}_{\mathrm{r}}^*{-}\boldsymbol{u}_3$, $\Delta \boldsymbol{u}_{\mathrm{f}}{=}\boldsymbol{u}_2{-}\boldsymbol{u}_3$ and $\mathrm{mid}\{\cdot\}$, the operator used for giving feasibility to the solution. Thereby, the resulting voltage vector $\boldsymbol{u}_{\mathrm{ap}}$ is given by the orthogonal projection of the relaxed solution to the hexagon's frontier. An illustrative example is shown in Fig. 4, in which the relaxed solution $\boldsymbol{u}_{\mathrm{r}2}$ is projected to border of the hexagon resulting in the red-line vector $\boldsymbol{u}_{\mathrm{ap}1}$. In this particular case $\Delta \boldsymbol{u}_{\mathrm{f}}{=}\boldsymbol{u}_{13}{-}\boldsymbol{u}_7$, and $\Delta \boldsymbol{u}_{\mathrm{r}}{=}\boldsymbol{u}_{\mathrm{r}}^*{-}\boldsymbol{u}_7$.

TABLE I
PARAMETERS OF THE SIMULATION.

Parameter	Description	Value
f_s	Sampling frequency	1 kHz
R_s	Stator resistance	57.61 mΩ
R_r	Rotor resistance	48.89 mΩ
L_{ls}	Stator leakage inductance	2.544 mH
L_{lr}	Rotor leakage inductance	1.881 mH
L_m	Main inductance	40.01 mH
p	Number of pole pairs	5
V_{dc}	dc-link voltage	5.2 kV
λ_{u0}	Weighting factor	0.2

The second saturation scheme scales the relaxed solution in order to put it on the inscribed circle of the outer hexagon of Fig. 4. Thus, the angular position of $\boldsymbol{u}_r^*$ is maintained leading to

$$\boldsymbol{u}_{\mathrm{ap}} = \boldsymbol{u}_{\mathrm{r}}^* \frac{V_{\max}}{\|\boldsymbol{u}_{\mathrm{r}}^*\|} = \frac{\sqrt{3}}{3} V_{dc} \frac{\boldsymbol{u}_{\mathrm{r}}^*}{\|\boldsymbol{u}_{\mathrm{r}}^*\|} \tag{19}$$

from which the duty-cycles are obtained considering the volt-second balancing as

$$\begin{bmatrix} d_2 & d_3 \end{bmatrix} = \begin{bmatrix} \boldsymbol{u}_2 & \boldsymbol{u}_3 \end{bmatrix}^{-1} \boldsymbol{u}_{\mathrm{ap}} \tag{20}$$

In consequence, this saturation method applies the green-line vector, $\boldsymbol{u}_{\mathrm{ap}2}$, for the relaxed solution $\boldsymbol{u}_{\mathrm{r}2}$ in Fig. 4.

IV. Simulation Results

To validate the proposed controller both steady-state and dynamic operating conditions are analysed. Simulations are carried out using PLECS software. For all cases, to balance the capacitor voltages, a methodology similar to the one presented in [12] is utilized where the duty cycles of the small vectors within a sequence a redistributed in order to balance v_{C1} and v_{C2} since the redundant vector have an opposite effect in the current injected to the middle point of the DC-link. The parameters of the system are summarized in Table I.

A. Steady-state performance

In this section, the following performance indexes are considered to evaluate the behaviour of the IM driven by the proposed controller: average torque tracking error, total demand distortion (TDD) of the torque defined by

$$T_{\mathrm{TDD}} = \frac{1}{T_{\mathrm{R}}} \sqrt{\sum_{h \neq 0} \hat{T}_h^2}, \tag{21}$$

and the average flux error over a fundamental cycle

$$E_\psi{=}\frac{1}{\sqrt{2}\Psi_{\mathrm{R}}} \sqrt{\sum_{k=1}^{N} \left(\boldsymbol{\psi}_s^*[k]{-}\frac{1}{T_s} \int_{kT_s}^{(k+1)T_s} \boldsymbol{\psi}_s(t)\, dt \right)^2}, \tag{22}$$

which is representative of the cost value obtained under the proposed control strategy. Finally, the harmonic spectrum of the stator currents is analysed for several speed references.

Fig. 5 shows the average tracking error and the TDD of the torque for a sampling frequency of 1 kHz. Both indexes are shown for the whole speed range considering two methods for predicting the stator flux: at the end of the switching cycle ($2T_0$), or at the end of the sub-cycle (T_0), as it is proposed

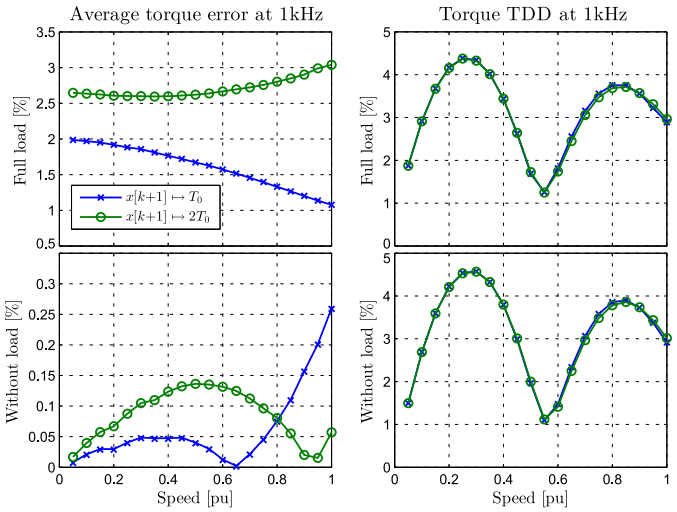

Fig. 5. Average torque error and T_{TDD} for the whole speed range considering no- and full-load operation.

in this work. As it can be seen, at full-load, the average torque tracking error is lesser for the whole speed range when the predictions are made at the end of the sub-cycle, thus controlling the average trajectory of the stator flux. Focusing on the torque TDD, the proposed prediction method leads to a slightly lower T_{TDD} for speed references above 0.55 p.u. and also for the rated speed. Notice that the resulting torque TDD, as defined in (21), is always below to 5%.

The waveforms of the $\alpha\beta$ components are shown for a speed reference of ω^*=0.55 pu, which according to Fig 7(a) corresponds to the speed for which the minimal value of E_ψ is achieved. Considering the resulting E_ψ for the whole speed range shown in Fig 7(a), it can be concluded that the controller regulates very well the average trajectory of $\boldsymbol{\psi}_s$.

The stator current harmonic spectrum is shown in Fig. 9 for several speed references considering no- and full-load. As it can be seen, the proposed MPC strategy shapes the harmonic spectrum. In addition, for all cases, the low order harmonics are below to 1.3% of the fundamental current at f_s=1 kHz.

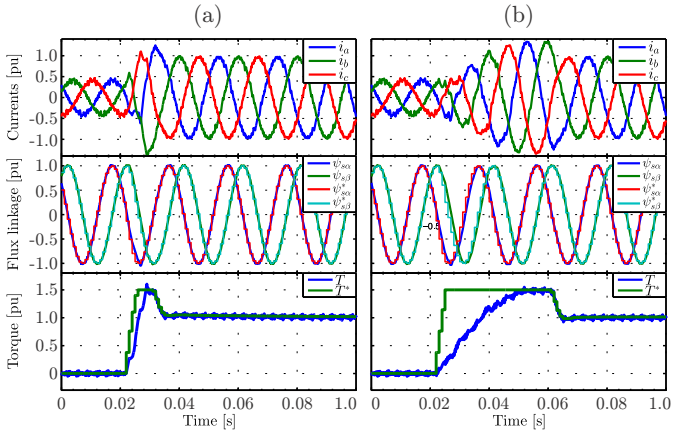

Fig. 6. Stator currents (i_{abc}), stator flux linkage components ($\psi_{s\alpha}, \psi_{s\beta}$) with their references, and torque using the saturation I (a) and saturation II (b).

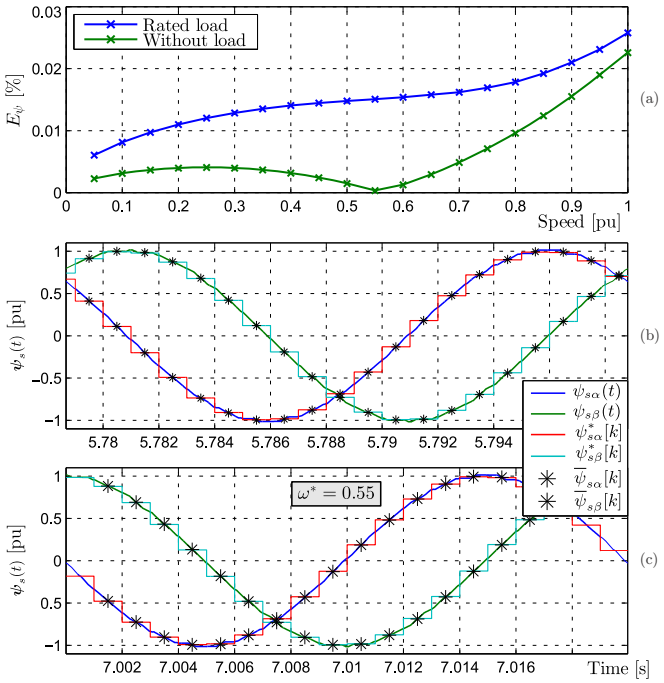

Fig. 7. Steady-state performance: (a) Average tracking error and stator flux waveforms without (b) and rated load (c) at $\omega^* = 0.55$[pu].

B. Dynamic performance

Fig. 6 compares the dynamic behaviour of the two saturation schemes analysed in this work when a rated torque load impact at rated speed is applied to the IM. As depicted in the torque waveforms of Fig. 6, the settling time of the proposed method is about 25% of the one obtained with the standard saturation method. As shown in Fig. 8, during this demanding transient condition, the proposed method uses the full available control region while the second method maintains the angular position of $\boldsymbol{u}_{\mathrm{r}}$ but limits its amplitude to the inscribed circle [see Fig. 8(b)].

C. Influence of the weighting factor λ_u

Fig. 10 compares the dynamic behaviour for two different weighting factors when a step down ω^*=0.5 $\rightarrow$ 0.25 pu. at rated torque is applied. As it can be seen, lower values of λ_u produce an oscillatory response, increasing both the current and torque ripple, which degrades the controller performance.

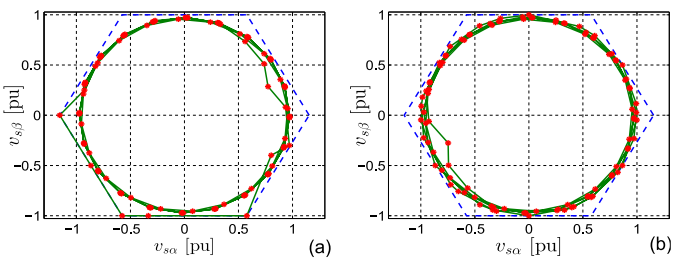

Fig. 8. Stator voltage trajectory using saturation I (a) and saturation II (b).

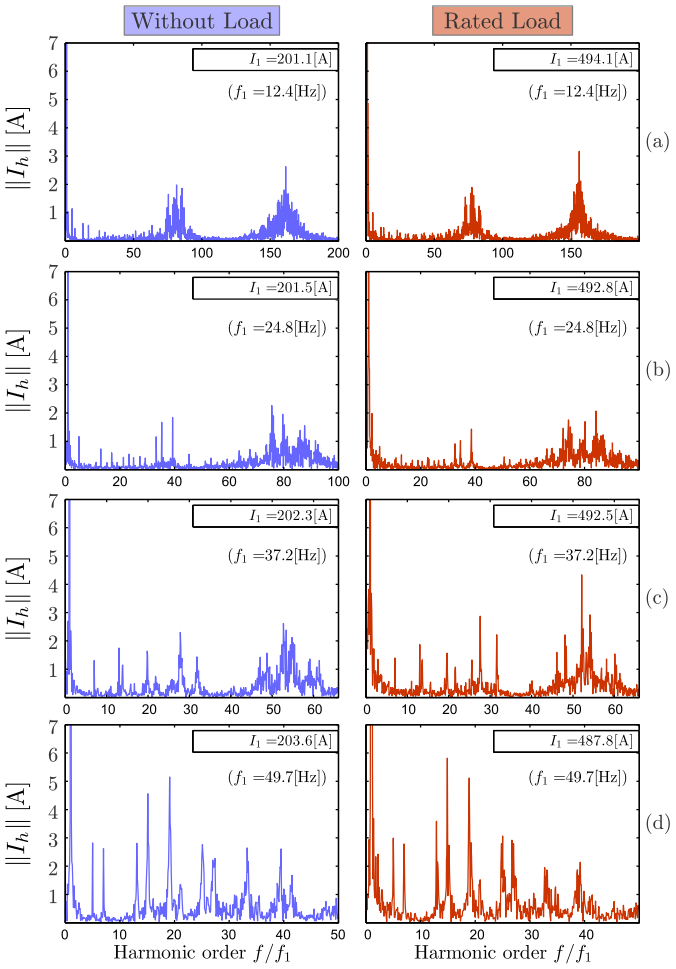

Fig. 9. Stator current harmonic spectrum at no- and rated-load for several speed references: (a) ω^*=0.25, (b) ω^*=0.5, (c) ω^*=0.75, (d) ω^*=1 pu.

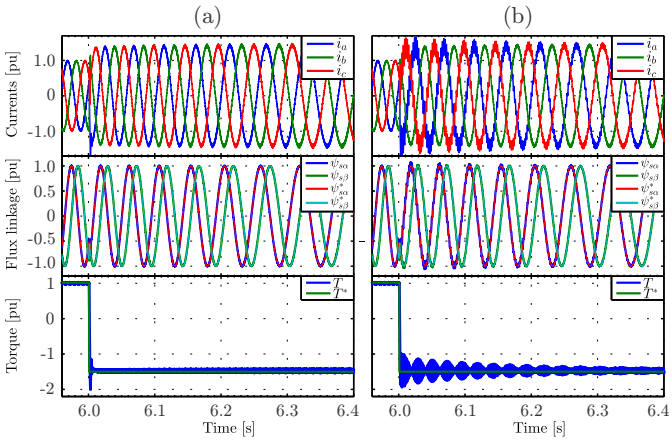

Fig. 10. Step down from ω^*=0.5→0.25 p.u. at rated load (a) λ_u=λ_{u0} and (b) λ_u=0.01λ_{u0}.

V. Conclusions

This paper proposes and validates a predictive stator flux controller to drive an induction machine using a 3L-NPC converter. The proposed control strategy reduces the average tracking and shapes the spectrum harmonic of the output voltage producing also a fixed switching frequency, which are the main disadvantages of standard FCS-MPC. In addition, a fast dynamic response is achieved. This strategy has been tested by simulation using a sampling frequency of 1 kHz.

The two saturation schemes discussed in this work allows giving feasibility to the relaxed solution. However, the suboptimal control action is only applied during transient operating conditions, such as load impact and changes on the speed reference. Therefore, the relaxed solution is the optimal solution during steady-state condition.

VI. Acknowledgements

The authors gratefully acknowledge financial support provided by Fondecyt Chile under Grant 1180879 and by Basal Project FB0008 “Advanced Center for Electrical and Electronic Engineering”. The work of A. Mora was supported by the Conicyt grants CONICYT-PCHA/Doctorado Nacional/2013-21130042 for Ph.D. studies.

References

[1] S. Vazquez, J. Rodriguez, M. Rivera, L. G. Franquelo, and M. Norambuena, “Model predictive control for power converters and drives: Advances and trends,” *IEEE Transactions on Industrial Electronics*, vol. 64, pp. 935–947, Feb 2017.

[2] J. Rodriguez, M. Kazmierkowski, J. Espinoza, P. Zanchetta, H. Abu-Rub, H. Young, and C. Rojas, “State of the art of finite control set model predictive control in power electronics,” *Industrial Informatics, IEEE Transactions on*, vol. 9, pp. 1003–1016, May 2013.

[3] R. P. Aguilera and D. E. Quevedo, “Predictive Control of Power Converters: Designs With Guaranteed Performance,” *IEEE Transactions on Industrial Informatics*, vol. 11, pp. 53–63, feb 2015.

[4] T. Geyer, “A Comparison of Control and Modulation Schemes for Medium-Voltage Drives: Emerging Predictive Control Concepts Versus PWM-Based Schemes,” *IEEE Transactions on Industry Applications*, vol. 47, pp. 1380–1389, may 2011.

[5] R. P. Aguilera, P. Lezana, and D. E. Quevedo, “Finite-control-set model predictive control with improved steady-state performance,” *IEEE Transactions on Industrial Informatics*, vol. 9, pp. 658–667, May 2013.

[6] T. Geyer and D. E. Quevedo, “Performance of multistep finite control set model predictive control for power electronics,” *IEEE Transactions on Power Electronics*, vol. 30, pp. 1633–1644, March 2015.

[7] R. Baidya, R. P. Aguilera, P. Acuña, S. Vazquez, and H. d. T. Mouton, “Multistep model predictive control for cascaded h-bridge inverters: Formulation and analysis,” *IEEE Transactions on Power Electronics*, vol. 33, pp. 876–886, Jan 2018.

[8] S. Vazquez, A. Marquez, R. Aguilera, D. Quevedo, J. I. Leon, and L. G. Franquelo, “Predictive optimal switching sequence direct power control for grid-connected power converters,” *IEEE Transactions on Industrial Electronics*, vol. 62, pp. 2010–2020, April 2015.

[9] L. Tarisciotti, P. Zanchetta, A. Watson, J. C. Clare, M. Degano, and S. Bifaretti, “Modulated Model Predictive Control for a Three-Phase Active Rectifier,” *IEEE Transactions on Industry Applications*, vol. 51, pp. 1610–1620, mar 2015.

[10] E. Fuentes, C. A. Silva, and R. M. Kennel, “Mpc implementation of a quasi-time-optimal speed control for a pmsm drive, with inner modulated-fs-mpc torque control,” *IEEE Transactions on Industrial Electronics*, vol. 63, pp. 3897–3905, June 2016.

[11] S. Vazquez, R. Aguilera, P. Acuna, J. Pou, J. Leon, L. Franquelo, and V. Agelidis, “Model Predictive Control for Single-Phase NPC Converters Based on Optimal Switching Sequences,” *IEEE Transactions on Industrial Electronics*, pp. 1–1, 2016.

[12] F. Donoso, A. Mora, R. Cárdenas, A. Angulo, D. Sáez, and M. Rivera, “Finite-set model-predictive control strategies for a 3l-npc inverter operating with fixed switching frequency,” *IEEE Transactions on Industrial Electronics*, vol. 65, pp. 3954–3965, May 2018.

[13] B. Wu, *High-Power Converters and AC Drives*. Wiley-IEEE Press, 2006.

[14] Y. Zhang, H. Yang, and B. Xia, “Model-predictive control of induction motor drives: Torque control versus flux control,” *IEEE Transactions on Industry Applications*, vol. 52, pp. 4050–4060, Sept 2016.

[15] S. Boyd and L. Vandenberghe, *Convex Optimization*. Cambridge University Press, 2004.